Search for a diffuse flux of astrophysical muon neutrinos with the IceCube 59-string configuration

M. G. Aartsen,[2] R. Abbasi,[29] M. Ackermann,[45] J. Adams,[15] J. A. Aguilar,[23] M. Ahlers,[29] D. Altmann,[22] C. Arguelles,[29] T. C. Arlen,[42] J. Auffenberg,[29] X. Bai,[33,*] M. Baker,[29] S. W. Barwick,[25] V. Baum,[30] R. Bay,[7] J. J. Beatty,[17,18] J. Becker Tjus,[10] K.-H. Becker,[44] S. BenZvi,[29] P. Berghaus,[45] D. Berley,[16] E. Bernardini,[45] A. Bernhard,[32] D. Z. Besson,[27] G. Binder,[8,7] D. Bindig,[44] M. Bissok,[1] E. Blaufuss,[16] J. Blumenthal,[1] D. J. Boersma,[43] C. Bohm,[36] D. Bose,[38] S. Böser,[11] O. Botner,[43] L. Brayeur,[13] H.-P. Bretz,[45] A. M. Brown,[15] R. Bruijn,[26] J. Casey,[5] M. Casier,[13] D. Chirkin,[29] A. Christov,[23] B. Christy,[16] K. Clark,[39] L. Classen,[22] F. Clevermann,[20] S. Coenders,[1] S. Cohen,[26] D. F. Cowen,[42,41] A. H. Cruz Silva,[45] M. Danninger,[36] J. Daughhetee,[5] J. C. Davis,[17] M. Day,[29] J. P. A. M. de André,[42] C. De Clercq,[13] S. De Ridder,[24] P. Desiati,[29] K. D. de Vries,[13] M. de With,[9] T. DeYoung,[42] J. C. Díaz-Vélez,[29] M. Dunkman,[42] R. Eagan,[42] B. Eberhardt,[30] B. Eichmann,[10] J. Eisch,[29] S. Euler,[1] P. A. Evenson,[33] O. Fadiran,[29] A. R. Fazely,[6] A. Fedynitch,[10] J. Feintzeig,[29] T. Feusels,[24] K. Filimonov,[7] C. Finley,[36] T. Fischer-Wasels,[44] S. Flis,[36] A. Franckowiak,[11] K. Frantzen,[20] T. Fuchs,[20] T. K. Gaisser,[33] J. Gallagher,[28] L. Gerhardt,[8,7] L. Gladstone,[29] T. Glüsenkamp,[45] A. Goldschmidt,[8] G. Golup,[13] J. G. Gonzalez,[33] J. A. Goodman,[16] D. Góra,[22] D. T. Grandmont,[21] D. Grant,[21] P. Gretskov,[1] J. C. Groh,[42] A. Groß,[32] C. Ha,[8,7] A. Haj Ismail,[24] P. Hallen,[1] A. Hallgren,[43] F. Halzen,[29] K. Hanson,[12] D. Hebecker,[11] D. Heereman,[12] D. Heinen,[1] K. Helbing,[44] R. Hellauer,[16] S. Hickford,[15] G. C. Hill,[2] K. D. Hoffman,[16] R. Hoffmann,[44] A. Homeier,[11] K. Hoshina,[29] F. Huang,[42] W. Huelsnitz,[16] P. O. Hulth,[36] K. Hultqvist,[36] S. Hussain,[33] A. Ishihara,[14] E. Jacobi,[45] J. Jacobsen,[29] K. Jagielski,[1] G. S. Japaridze,[4] K. Jero,[29] O. Jlelati,[24] B. Kaminsky,[45] A. Kappes,[22] T. Karg,[45] A. Karle,[29] M. Kauer,[29] J. L. Kelley,[29] J. Kiryluk,[37] J. Kläs,[44] S. R. Klein,[8,7] J.-H. Köhne,[20] G. Kohnen,[31] H. Kolanoski,[9] L. Köpke,[30] C. Kopper,[29] S. Kopper,[44] D. J. Koskinen,[19] M. Kowalski,[11] M. Krasberg,[29] A. Kriesten,[1] K. Krings,[1] G. Kroll,[30] J. Kunnen,[13] N. Kurahashi,[29] T. Kuwabara,[33] M. Labare,[24] H. Landsman,[29] M. J. Larson,[40] M. Lesiak-Bzdak,[37] M. Leuermann,[1] J. Leute,[32] J. Lünemann,[30] O. Macías,[15] J. Madsen,[35] G. Maggi,[13] R. Maruyama,[29] K. Mase,[14] H. S. Matis,[8] F. McNally,[29] K. Meagher,[16] M. Merck,[29] T. Meures,[12] S. Miarecki,[8,7] E. Middell,[45] N. Milke,[20] J. Miller,[13] L. Mohrmann,[45] T. Montaruli,[23] R. Morse,[29] R. Nahnhauer,[45] U. Naumann,[44] H. Niederhausen,[37] S. C. Nowicki,[21] D. R. Nygren,[8] A. Obertacke,[44] S. Odrowski,[21] A. Olivas,[16] A. Omairat,[44] A. O'Murchadha,[12] T. Palczewski,[40] L. Paul,[1] J. A. Pepper,[40] C. Pérez de los Heros,[43] C. Pfendner,[17] D. Pieloth,[20] E. Pinat,[12] J. Posselt,[44] P. B. Price,[7] G. T. Przybylski,[8] M. Quinnan,[42] L. Rädel,[1] M. Rameez,[23] K. Rawlins,[3] P. Redl,[16] R. Reimann,[1] E. Resconi,[32] W. Rhode,[20] M. Ribordy,[26] M. Richman,[16] B. Riedel,[29] S. Robertson,[2] J. P. Rodrigues,[29] C. Rott,[38] T. Ruhe,[20] B. Ruzybayev,[33] D. Ryckbosch,[24] S. M. Saba,[10] H.-G. Sander,[30] M. Santander,[29] S. Sarkar,[19,34] K. Schatto,[30] F. Scheriau,[20] T. Schmidt,[16] M. Schmitz,[20] S. Schoenen,[1] S. Schöneberg,[10] A. Schönwald,[45] A. Schukraft,[1,†] L. Schulte,[11] O. Schulz,[32] D. Seckel,[33] Y. Sestayo,[32] S. Seunarine,[35] R. Shanidze,[45] C. Sheremata,[21] M. W. E. Smith,[42] D. Soldin,[44] G. M. Spiczak,[35] C. Spiering,[45] M. Stamatikos,[17,‡] T. Stanev,[33] N. A. Stanisha,[42] A. Stasik,[11] T. Stezelberger,[8] R. G. Stokstad,[8] A. Stößl,[45] E. A. Strahler,[13] R. Ström,[43] N. L. Strotjohann,[11] G. W. Sullivan,[16] H. Taavola,[43] I. Taboada,[5] A. Tamburro,[33] A. Tepe,[44] S. Ter-Antonyan,[6] G. Tešić,[42] S. Tilav,[33] P. A. Toale,[40] M. N. Tobin,[29] S. Toscano,[29] M. Tselengidou,[22] E. Unger,[10] M. Usner,[11] S. Vallecorsa,[23] N. van Eijndhoven,[13] A. Van Overloop,[24] J. van Santen,[29] M. Vehring,[1] M. Voge,[11] M. Vraeghe,[24] C. Walck,[36] T. Waldenmaier,[9] M. Wallraff,[1] Ch. Weaver,[29] M. Wellons,[29] C. Wendt,[29] S. Westerhoff,[29] B. Whelan,[2] N. Whitehorn,[29] K. Wiebe,[30] C. H. Wiebusch,[1] D. R. Williams,[40] H. Wissing,[16] M. Wolf,[36] T. R. Wood,[21] K. Woschnagg,[7] D. L. Xu,[40] X. W. Xu,[6] J. P. Yanez,[45] G. Yodh,[25] S. Yoshida,[14] P. Zarzhitsky,[40] J. Ziemann,[20] S. Zierke,[1] and M. Zoll[36]

(IceCube Collaboration)

[1]*III. Physikalisches Institut, RWTH, Aachen University, D-52056 Aachen, Germany*
[2]*School of Chemistry & Physics, University of Adelaide, Adelaide, South Australia 5005, Australia*
[3]*Department of Physics and Astronomy, University of Alaska Anchorage, 3211 Providence Dr., Anchorage, Alaska 99508, USA*
[4]*CTSPS, Clark-Atlanta University, Atlanta, Georgia 30314, USA*
[5]*School of Physics and Center for Relativistic Astrophysics, Georgia Institute of Technology, Atlanta, Georgia 30332, USA*
[6]*Department of Physics, Southern University, Baton Rouge, Louisiana 70813, USA*
[7]*Department of Physics, University of California, Berkeley, California 94720, USA*
[8]*Lawrence Berkeley National Laboratory, Berkeley, California 94720, USA*
[9]*Institut für Physik, Humboldt-Universität zu Berlin, D-12489 Berlin, Germany*
[10]*Fakultät für Physik & Astronomie, Ruhr-Universität Bochum, D-44780 Bochum, Germany*
[11]*Physikalisches Institut, Universität Bonn, Nussallee 12, D-53115 Bonn, Germany*
[12]*Science Faculty CP230, Université Libre de Bruxelles, B-1050 Brussels, Belgium*

 © 2014 American Physical Society

[13]*Vrije Universiteit Brussel, Dienst ELEM, B-1050 Brussels, Belgium*
[14]*Department of Physics, Chiba University, Chiba 263-8522, Japan*
[15]*Department of Physics and Astronomy, University of Canterbury, Private Bag 4800, Christchurch 8140, New Zealand*
[16]*Department of Physics, University of Maryland, College Park, Maryland 20742, USA*
[17]*Department of Physics and Center for Cosmology and Astro-Particle Physics, Ohio State University, Columbus, Ohio 43210, USA*
[18]*Department of Astronomy, Ohio State University, Columbus, Ohio 43210, USA*
[19]*Niels Bohr Institute, University of Copenhagen, DK-2100 Copenhagen, Denmark*
[20]*Department of Physics, TU Dortmund University, D-44221 Dortmund, Germany*
[21]*Department of Physics, University of Alberta, Edmonton, Alberta T6G 2E1, Canada*
[22]*Erlangen Centre for Astroparticle Physics, Friedrich-Alexander-Universität Erlangen-Nürnberg, D-91058 Erlangen, Germany*
[23]*Département de physique nucléaire et corpusculaire, Université de Genève, CH-1211 Genève, Switzerland*
[24]*Department of Physics and Astronomy, University of Gent, B-9000 Gent, Belgium*
[25]*Department of Physics and Astronomy, University of California, Irvine, California 92697, USA*
[26]*Laboratory for High Energy Physics, École Polytechnique Fédérale, CH-1015 Lausanne, Switzerland*
[27]*Department of Physics and Astronomy, University of Kansas, Lawrence, Kansas 66045, USA*
[28]*Department of Astronomy, University of Wisconsin, Madison, Wisconsin 53706, USA*
[29]*Department of Physics, Wisconsin IceCube Particle Astrophysics Center, University of Wisconsin, Madison, Wisconsin 53706, USA*
[30]*Institute of Physics, University of Mainz, Staudinger Weg 7, D-55099 Mainz, Germany*
[31]*Université de Mons, 7000 Mons, Belgium*
[32]*T.U. Munich, D-85748 Garching, Germany*
[33]*Department of Physics and Astronomy, Bartol Research Institute, University of Delaware, Newark, Delaware 19716, USA*
[34]*Department of Physics, University of Oxford, 1 Keble Road, Oxford OX1 3NP, United Kingdom*
[35]*Department of Physics, University of Wisconsin, River Falls, Wisconsin 54022, USA*
[36]*Oskar Klein Centre, Department of Physics, Stockholm University, SE-10691 Stockholm, Sweden*
[37]*Department of Physics and Astronomy, Stony Brook University, Stony Brook, New York 11794-3800, USA*
[38]*Department of Physics, Sungkyunkwan University, Suwon 440-746, Korea*
[39]*Department of Physics, University of Toronto, Toronto, Ontario M5S 1A7, Canada*
[40]*Department of Physics and Astronomy, University of Alabama, Tuscaloosa, Alabama 35487, USA*
[41]*Department of Astronomy and Astrophysics, Pennsylvania State University, University Park, Pennsylvania 16802, USA*
[42]*Department of Physics, Pennsylvania State University, University Park, Pennsylvania 16802, USA*
[43]*Department of Physics and Astronomy, Uppsala University, Box 516, S-75120 Uppsala, Sweden*
[44]*Department of Physics, University of Wuppertal, D-42119 Wuppertal, Germany*
[45]*DESY, D-15735 Zeuthen, Germany*

(Received 27 November 2013; published 25 March 2014)

A search for high-energy neutrinos was performed using data collected by the IceCube Neutrino Observatory from May 2009 to May 2010, when the array was running in its 59-string configuration. The data sample was optimized to contain muon neutrino induced events with a background contamination of atmospheric muons of less than 1%. These data, which are dominated by atmospheric neutrinos, are analyzed with a global likelihood fit to search for possible contributions of prompt atmospheric and astrophysical neutrinos, neither of which have yet been identified. Such signals are expected to follow a harder energy spectrum than conventional atmospheric neutrinos. In addition, the zenith angle distribution differs for astrophysical and atmospheric signals. A global fit of the reconstructed energies and directions of observed events is performed, including possible neutrino flux contributions for an astrophysical signal and atmospheric backgrounds as well as systematic uncertainties of the experiment and theoretical predictions. The best fit yields an astrophysical signal flux for $\nu_\mu + \bar{\nu}_\mu$ of $E^2 \cdot \Phi(E) = 0.25 \times 10^{-8}$ GeV cm^{-2} s^{-1} sr^{-1},

[*]Also at Physics Department, South Dakota School of Mines and Technology, Rapid City, SD 57701, USA.
[†]Corresponding author.
schukraft@physik.rwth-aachen.de
[‡]Also at NASA Goddard Space Flight Center, Greenbelt, MD 20771, USA.

and a zero prompt component. Although the sensitivity of this analysis for astrophysical neutrinos surpasses the Waxman and Bahcall upper bound, the experimental limit at 90% confidence level is a factor of 1.5 above at a flux of $E^2 \cdot \Phi(E) = 1.44 \times 10^{-8}$ GeV cm^{-2} s^{-1} sr^{-1}.

DOI: 10.1103/PhysRevD.89.062007 PACS numbers: 95.85.Ry, 29.40.Ka, 95.55.Vj, 98.70.Sa

I. INTRODUCTION

High-energy neutrinos are believed to be ideal cosmic messenger particles to use to discover the enigmatic sources of high-energy cosmic rays. They are generated from the weak decay of charged mesons, in particular pions and kaons produced in hadronic interactions in, or close to, the sources. In generic scenarios [1–3] these neutrinos are expected to exhibit the same hard energy spectrum as the accelerated parent particles, yielding a typical differential spectrum $\Phi(E) \propto E^{-2}$.

To date, no cosmic high-energy neutrino sources have been found [4]. This motivates the complementary approach of a search for a diffuse flux of astrophysical neutrinos [5]. A cumulative flux is composed of the integrated flux of all neutrino sources and could be detected even if the individual source fluxes are below the detection threshold, as long as the source population is large. Such a scenario is in particular imaginable for extragalactic sources, e.g. active galactic nuclei, which are among the candidate sources of ultra high-energy cosmic rays and could produce a detectable neutrino signal in the energy region between 10 TeV and 10 PeV [1,2,6].

The IceCube Neutrino Observatory is sensitive to diffuse fluxes of high-energy neutrinos of different flavors [7–10]. With the IceCube detector, two basic event signatures can be distinguished: track-like patterns of detected Cherenkov light, which originate from muons produced in charged-current interactions of muon neutrinos (muon channel), and spherical hit patterns which originate from the hadronic cascade at the vertex of neutrino interactions or the electromagnetic cascade of electrons from charged current interactions of electron neutrinos (cascade channel). IceCube has recently reported evidence for high-energy extraterrestrial neutrinos [9] in an analysis of data taken with the IceCube detector configurations of 79 and 86 strings. This excess of high-energy events was found by analyzing events with their interaction vertex contained in the detector and is dominated by cascade-like events. The analysis presented in this publication searches for a high-energy diffuse astrophysical neutrino signal in the muon channel with the 59-string configuration, and is improved with respect to the analysis of the 40-string configuration [10]. This analysis is mostly sensitive to charged-current interactions of muon neutrinos in the energy regime from a few TeV to several tens of PeV. A small sensitivity to charged-current interactions of tau neutrinos remains via taus decaying into muons. The field of view of this analysis is restricted to upward-going neutrinos in order to reject the dominant background of atmospheric muons (see Sec. II). The analyses of neutrino induced muon tracks and contained cascade-like events are technically and conceptually complementary: the cascade-like channel can achieve a 4π acceptance, if atmospheric background muons which enter the detector from above can be identified at the detector boundary and vetoed. However, this background rejection technique introduces a relatively high energy threshold and reduces the effective volume, and therefore the event statistics, compared to the muon channel. On the contrary, a pure sample of neutrino induced upward-going muon tracks allows the search for an astrophysical diffuse neutrino signal and a high-statistics measurement of the lower energy atmospheric neutrino background at the same time. Hence, this analysis of upward-going muon tracks verifies the background estimation of analyses in the cascade-like channel such as [9].

The main background to this search is the flux of atmospheric neutrinos, which is produced in cosmic-ray interactions with the Earth's atmosphere. The conventional atmospheric muons and neutrinos are produced in the decay of charged pions and kaons. Their energy spectrum is about one power steeper than the spectrum of the parent cosmic rays at Earth, due to the energy dependent competition between meson decay and interaction in the atmosphere. It is a power law with a spectral index of typically $\gamma = 3.7$.

An additional atmospheric component is the flux of prompt atmospheric neutrinos: such neutrinos are produced in the decay of heavier mesons containing a charm quark. The cross sections for their production are small and therefore their contribution is only relevant at higher energies, where the conventional component is suppressed below this level [11–13]. These heavy mesons have such short lifetimes that they immediately decay, rather than interact, which causes prompt neutrinos to follow the energy spectrum of the parent cosmic rays. They are a background for astrophysical neutrino searches at high energies, and have not yet been experimentally identified. Theoretical predictions of absolute fluxes are highly uncertain, mainly due to uncertainties in the parton distribution functions at very small values of Bjorken–x, which cannot be measured by collider experiments.

The different energy spectra of astrophysical, prompt and conventional atmospheric neutrinos are the main criteria for distinguishing the different components in the neutrino data sample measured with IceCube. This is illustrated in Fig. 1, which shows the expected energy

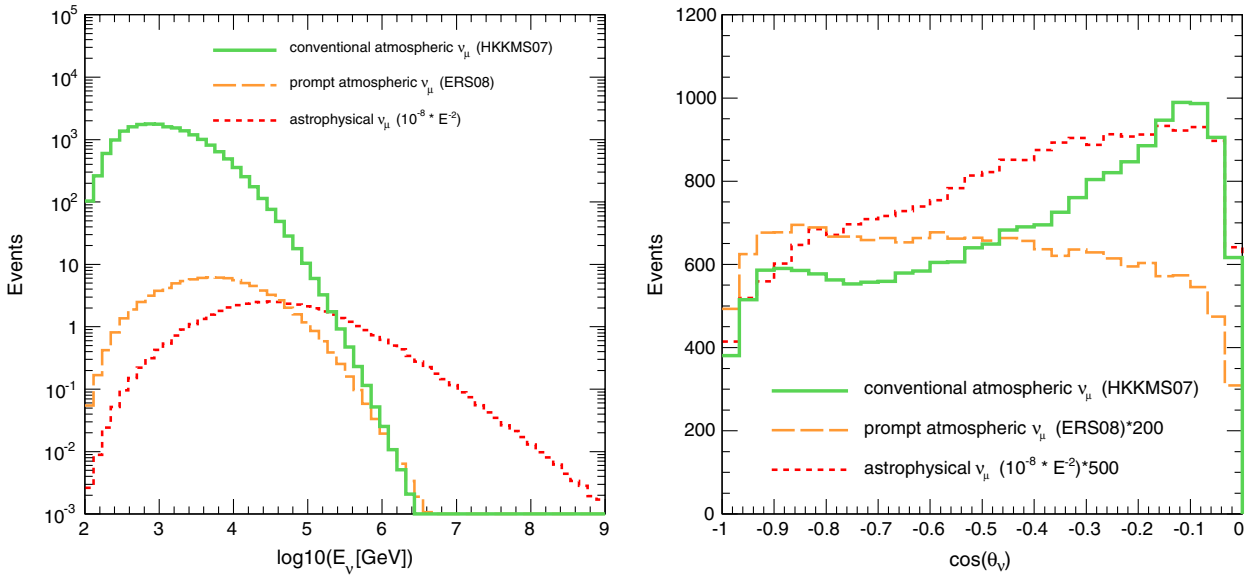

FIG. 1 (color online). Distribution of primary neutrino energies and zenith angles for conventional atmospheric [14,15], prompt atmospheric [13] and astrophysical $\nu_\mu + \bar{\nu}_\mu$ expected in the runtime of 348.1 days, folded with the detection efficiency of this analysis. Note, the flux normalization of the latter two are multiplied by factors of 200 and 500 for better visibility in the right figure.

and zenith angle distributions for the neutrino event selection used here (see Sec. II).

An additional criterion is the zenith angle dependence: conventional atmospheric neutrinos exhibit a characteristic distribution with a maximum at the horizon. The reason is the angle dependent path lengths of their parent mesons in the atmosphere, which determine their probability to decay and produce neutrinos before reaching the detector. As mentioned above, the mesons which produce prompt atmospheric neutrinos decay immediately, and therefore the prompt neutrinos are almost isotropically distributed. Assuming an isotropic distribution of astrophysical sources, the observed zenith angle distribution of astrophysical events is modified by the detector angular acceptance and the energy dependent absorption probability of neutrinos inside the Earth, which increases with energy. The absorption effect is stronger for astrophysical neutrinos than for prompt and conventional atmospheric neutrinos, due to their harder energy spectrum.

The connection between cosmic rays and astrophysical neutrinos permits an estimation of an upper bound for such a diffuse neutrino flux. The normalization of the neutrino flux to the observed cosmic-ray flux under the assumption of optimistic parameters for the efficiency of hadronic neutrino production in optically thin sources without reacceleration of decaying parent particles leads to an upper bound of $E_\nu^2 \cdot \Phi(E_\nu) \sim 10^{-8}$ GeV cm^{-2} s^{-1} sr^{-1}, as calculated by Waxman and Bahcall [16,17]. Other model predictions for diffuse neutrino fluxes are based on the observed photon flux at different wavelengths from different experiments and can be above or below this upper bound (see Sec. V). The analysis presented in this paper reaches a sensitivity below the Waxman-Bahcall upper bound.

This paper is organized as follows: Sec. II describes the IceCube detector and the selection of upward-going muon neutrino events. The likelihood fit, which was chosen as an analysis method, and the treatment of systematic uncertainties in this fit are explained in Sec. III and Sec. IV. Section V presents and discusses the results, and the analysis is summarized in Sec. VI.

II. ICECUBE DETECTOR AND DATA SELECTION

IceCube is a neutrino detector located at the geographic South Pole [18]. In neutrino interactions with nuclei, secondary particles are produced, which travel faster than the speed of light in the Antarctic ice and therefore emit Cherenkov light. These photons are detected by optical sensors deployed in the Antarctic ice. In the final detector configuration, the digital optical modules (DOMs) are arranged on 86 vertical strings of 60 sensors, each spread over depths between 1450 and 2450 m with vertical distances of 17 m between sensors. Seventy-eight strings have a horizontal spacing of about 125 m and span a hexagon of a surface area of roughly 1 km^2. A further eight strings, together with the seven surrounding IceCube strings, form the more densely instrumented central DeepCore detector [19]. The IceCube detector was completed in December 2010. The analysis presented here was performed with data taken between May 2009 and May 2010, when IceCube was still under construction and consisted of 59 strings.

The digital optical modules contain a photomultiplier tube (PMT) housed in a borosilicate glass pressure sphere. The PMT quantum efficiency as well as the transparency of the glass and the optical gel make the module most sensitive to wavelengths in the ultraviolet and blue regions [20]. This is optimal for the Cherenkov radiation filtered through Antarctic ice. If a trigger condition is fulfilled, the recorded waveforms are digitized and transferred to the surface. The quantities, which are extracted from the measured waveforms of each DOM, are the total number and arrival times of PMT photoelectron pulses, corresponding to the detected Cherenkov photons (see Fig. 2). This information is used for the reconstruction of the direction and estimation of the energy of the secondary particles, which is highly correlated to the initial neutrino direction and energy [21–23].

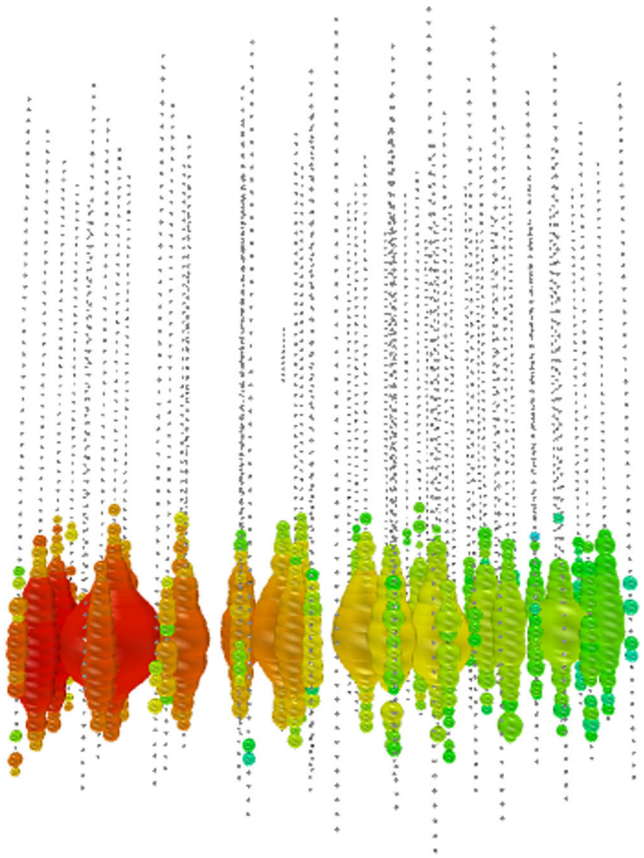

FIG. 2 (color online). Event view of the highest-energy neutrino event observed in this analysis. The grey dots mark IceCube DOMs. DOMs hit by photons are shown in color. The color code indicates the photon arrival time with red colors marking early times and green colors standing for late times. The radius of the DOMs correlates with the observed charge in the PMT. In this projection, the muon is traveling from left to right. The reconstructed zenith angle of this event is $91.2° \pm 0.1°$ and the reconstructed, truncated muon energy loss is $\log(dE/dx[\mathrm{GeV/m}]) = 1.37$ within the detection volume. Assuming the best-fit energy spectrum from this analysis (see Fig. 4), this event most likely originated from a neutrino of energy 500 TeV–1 PeV, producing a muon that passed through the detector with an energy of about 400 TeV.

The typical trigger condition for high-energy neutrino analyses in IceCube requires at least eight sensors recording light within a time window of 5 μs. The triggering sensors must be in a local coincidence with either of their neighboring or next-to-nearest neighboring sensors. Most of the triggers come from atmospheric muons, which are produced in cosmic-ray air showers in the Earth's atmosphere and are the main background in the search for neutrinos. With the 59-string configuration, the trigger rate for atmospheric muons was 1500 Hz and initially outnumbered the rate of atmospheric neutrino induced tracks by more than five orders of magnitude (see Table II). A significant contribution to the atmospheric muon trigger rate comes from muons from coincident but independent air showers (coincident muons), which are particulary challenging to identify. The analysis requires a neutrino sample with a very low background contamination of atmospheric muons while retaining as many high-energy neutrino events as possible. It is optimized for the detection of through-going muons originating from muon neutrino charged-current interactions, which cause a track-like signature in the detector. The separation of neutrino induced events from atmospheric muons is based on several steps: in the online processing at the South Pole, potentially interesting events are selected and transmitted to the data centers in the North via satellite. During the offline processing, more advanced reconstructions are performed and the data stream is further reduced through a preselection of highly energetic tracks. A high-purity muon neutrino sample is finally obtained through a series of quality cuts on reconstruction quality parameters. These steps are described in the following paragraphs.

At the South Pole, isolated noise pulses are excluded from the reconstruction. An online filter criterion optimized for track-like signatures reduces the data stream and selects high-energy muon candidate events. It requires a minimum amount of detected total charge and a minimum quality of a likelihood track reconstruction. The rejection of atmospheric muons takes advantage of the fact that muons are absorbed in matter, while neutrinos are able to traverse the Earth and are the only particles arriving at the detector from below. Therefore, the filter criteria depend on the result of a fast first-guess angular reconstruction algorithm (Linefit) and are stronger for downward-going than for upward-going events. When transmitted to the North, atmospheric muons still dominate the neutrinos by a factor 10^4.

During the offline processing, further reconstructions, in particular an iterative likelihood track fit including the number of detected photons [multi-photoelectron (MPE) likelihood], are performed. As a preselection of high-energy neutrino events, the field of view of the analysis is completely restricted to the upward-going region with zenith angles $\theta > 90°$ (MPE likelihood fit). Additionally, a

minimum number of hit sensors sufficiently close enough to the reconstructed track hypothesis to observe unscattered Cherenkov photons emitted by the primary muon is required. In addition, the event's hit pattern is searched for subsets of causally connected pulses in order to remove remaining noise pulses and to identify pulses from coincident particles. For $\lesssim$50% of the atmospheric muon dominated experimental data or $\lesssim$30% of simulated atmospheric neutrino events, subsets of pulses are found which are not causally connected with the main cluster of pulses. These pulses will therefore be ignored in the following high-level track and energy reconstructions.

The high-level event selection is developed through a comparison of Monte Carlo generated neutrino event signatures and atmospheric muon signatures. Neutrino events are generated and propagated through the Earth to a region surrounding the detector where their interactions in the rock and ice are simulated [24]. Neutrino induced muons are then tracked into and through the detector taking account of stochastic and continuous energy losses [25]. Cherenkov light from charged particles is propagated to the optical modules [26] taking account of scattering and absorption in the ice [27,28]. Finally, the generation of the signal as a function of time in the optical module is simulated in detail. The background of atmospheric muons is simulated with the air shower simulation software CORSIKA [29] and from there on the CORSIKA output is passed through the same simulation chain as the neutrinos.

Generated neutrino events are reweighted to a primary astrophysical or atmospheric neutrino spectrum of choice. In this analysis, the baseline model to describe the incoming flux of conventional atmospheric neutrinos is based on the model HKKMS07 [14]. The calculations in Refs. [14,30] extend only to $E_\nu = 10$ TeV. In previous IceCube analyses [10,31] these results have been extrapolated to higher energy by fitting a standard parametrization [32],

$$\Phi(E_\nu) \simeq \Phi_0 \cdot E_\nu^{-\gamma} \cdot \left(\frac{A_{\pi\nu}}{1 + B_{\pi\nu} E_\nu \cos(\theta^*)/\epsilon_\pi} + \frac{A_{K\nu}}{1 + B_{K\nu} E_\nu \cos(\theta^*)/\epsilon_K} \right), \quad (1)$$

to the published neutrino calculations below 10 TeV. In this equation, θ^* is the zenith angle where the neutrinos are produced, taking account of the curvature of the Earth [33]. The parameters Φ_0, A and B are free fit parameters, the spectral index is $\gamma = 2.7$, and the critical energies are $\epsilon_\pi = 115$ GeV and $\epsilon_K = 850$ GeV. Such an extrapolation does not account for the knee in which the overall spectrum of the cosmic rays becomes steeper between 1 and 10 PeV.

This analysis extends to PeV neutrino energies and therefore the steepening at the knee has to be accounted for. Since neutrino production occurs at the level of interactions of individual nucleons and mesons, a parametrization of the evolution of the elemental composition through the knee region is needed. Two different parametrizations, H3a of Ref. [15] and a modified version of the poly-gonato parametrization [34] in which its galactic component is supplemented with an extragalactic component of the form of Ref. [15], are considered. The effect of the knee is implemented by folding the yield of neutrinos per primary nucleon with the primary spectrum of nucleons, as described in the Appendix. The prompt atmospheric neutrino flux is estimated according to the prediction by Enberg *et al.* (ERS08) [13] as a baseline model, which has also been modified at high energies to take into account the cosmic-ray flux parametrizations of H3a and poly-gonato (see the Appendix).

After the offline processing and the preselection of high-energy upward-going tracks, the remaining backgrounds are misreconstructed events, often caused by coincident muons or muons passing outside the instrumented volume, which, despite being truly downward going, are reconstructed as upward going. Such background events are removed by selecting only upward-going events of high offline-reconstruction quality, while retaining as many high-energy candidate neutrino induced tracks as possible. This is accomplished by setting quality conditions on a number of parameters. The parameters are described in Ref. [21,35] and have their origin in five different ways of identifying events which are likely to have been poorly reconstructed. These parameters and the selection criteria are listed below and summarized in Table I.

(1) The upward-going condition, $\theta > 90°$, is required to be satisfied for the zenith angles found in the two angular reconstruction algorithms, MPE likelihood fit and Linefit.

(2) A minimum track reconstruction quality is required based on the reduced negative log-likelihood at the minimum $r \log l = -\log \mathcal{L}/(N_{\mathrm{ch}} - 5)$, where N_{ch} is the number of hit sensors in the event. Additionally, the angular error estimation of the MPE likelihood fit $\sigma_{\mathrm{paraboloid}}$ has to be smaller than 5°. Directional consistency between the two reconstruction algorithms, MPE likelihood fit and Linefit, is required through a condition that the difference between the zenith angles obtained from each algorithm ψ satisfies $\psi \leq 15°$.

(3) The rejection of misreconstructed atmospheric muons is improved by a cut on the likelihood ratio of the reconstructed solution to a second reconstruction which is forced to a downward-going track and in which the likelihood is weighted with a Bayesian prior describing the probability that a downward-going muon is expected at that reconstructed zenith angle. In addition, individual reconstructions are performed on the hit pattern split in half based on geometry or time. All reconstructions of each split hit pattern have to fulfill $\theta > 80°$.

TABLE I. List of event selection criteria and corresponding passing efficiencies. The passing efficiencies are given with respect to the previous step. The astrophysical neutrino flux is estimated assuming an E^{-2} power law, and the conventional atmospheric neutrino flux is based on the prediction by Honda *et al.* (HKKMS07) [14] including the modification of the H3a cosmic-ray flux parametrization [15]. (Conv. = conventional, Atms. = atmospheric).

Group	Selection criterion	Passing efficiencies		
		Atms. μ (coincident)	Astrophysical	Conv. atms. ν_μ
1	$\theta(\mathrm{MPE}) > 90°$	95% (95%)	98%	97%
	$\theta(\mathrm{Linefit}) > 90°$	65% (57%)	92%	91%
2	$r \log l < 11$	33% (42%)	93%	75%
	$\sigma_{\mathrm{paraboloid}} < 5°$	19% (37%)	77%	67%
	$\psi(\mathrm{Linefit}, \mathrm{MPE}) < 15°$	39% (49%)	90%	92%
3	$\log(\frac{\mathcal{L}_{\mathrm{SPE}}}{\mathcal{L}_{\mathrm{Bayesian}}}) > 29$	22% (30%)	89%	67%
	$\min(\theta_{\mathrm{geo1}}, \theta_{\mathrm{geo2}}, \theta_{\mathrm{time1}}, \theta_{\mathrm{time2}}) > 80°$	3% (2%)	84%	67%
4	$N_{\mathrm{dir}} > 6$	3% (2%)	97%	94%
	$L_{\mathrm{dir}} > 250$ m	93% (91%)	98%	97%
	$\lvert S_{\mathrm{dir}} \rvert < 0.45$	30% (43%)	97%	96%
5	-450 m $< z_{\mathrm{COG}} < 400$ m	87% (96%)	96%	97%

(4) In order to guarantee a matching between the track hypothesis and the measured hit pattern, a minimum number of direct hits N_{dir}, i.e. pulses that are recorded within a time window of -15 to 75 ns of the geometrically expected arrival time and therefore attributed to unscattered photons, is required. Furthermore, the direct length L_{dir}, which is determined by the projection of the direct hits on the reconstructed track, has to exceed a certain minimum length. Additionally, these direct hits have to occur continuously along the reconstructed track, quantified by the smoothness variable S_{dir}.

(5) Background events, which may pass above or below the detector and are very hard to reconstruct in direction and energy, are rejected by the requirement that the position of the center of gravity of hit optical modules in the vertical direction (z_{COG}) is not at the top or bottom of the detector.

The passing efficiencies are summarized in Table II. The data selection was optimized keeping the signal region of the experimental data blind in order to avoid introducing a bias in the analysis. The signal region is defined as the 5% of events with the highest reconstructed energy loss.

As listed in Table II, the final experimental data sample consists of 21943 events acquired within a total livetime of 348.1 days. The sample is expected to be dominated by conventional atmospheric neutrinos with an expected number of 21844 events based on the HKKMS07 model, including the modification of the H3a cosmic-ray flux parametrization. The expected number of prompt neutrinos is 91 for the model ERS08 modified to correspond to the H3a cosmic-ray flux parametrization. An astrophysical flux

TABLE II. Measured and expected event rates in Hz for the IceCube 59-string data stream with a total livetime of 348.1 days. Atmospheric muon background expectations are based on CORSIKA simulation. Predictions for conventional atmospheric neutrinos are based on the prediction by Honda *et al.* (HKKMS07) [14] including the modification of the H3a cosmic-ray flux parametrization [15] and scaled to the best-fit nuisance parameters obtained later in this analysis (see Sec. V). The prompt atmospheric neutrino flux given in the table corresponds to the prediction ERS08 [13] and has also been modified based on the H3a parametrization. (Conv. = conventional, Atms. = atmospheric).

	Experimental data	Atms. μ CORSIKA total (coincident)	Astrophysical ν_μ ($\nu_\mu + \nu_\tau$) 10^{-8} GeV cm^{-2} s^{-1} sr^{-1} $\cdot E^{-2}$	Conv. atms. ν_μ HKKMS07 + H3a best fit	Prompt atms. ν_μ ERS08 + H3a + H3a
Trigger level [Hz]	1.5×10^3	1.4×10^3		2.4×10^{-2}	
Satellite transmitted [Hz]	35.2	30.2		8×10^{-3}	
At final level [Hz]	7.3×10^{-4}	9.6×10^{-7} (7.0×10^{-7})	1.5×10^{-6} (1.7×10^{-6})	7.2×10^{-4}	3.0×10^{-6}
#ν at final level in 348 days	21943	29 (21)	46 (50)	21844	91

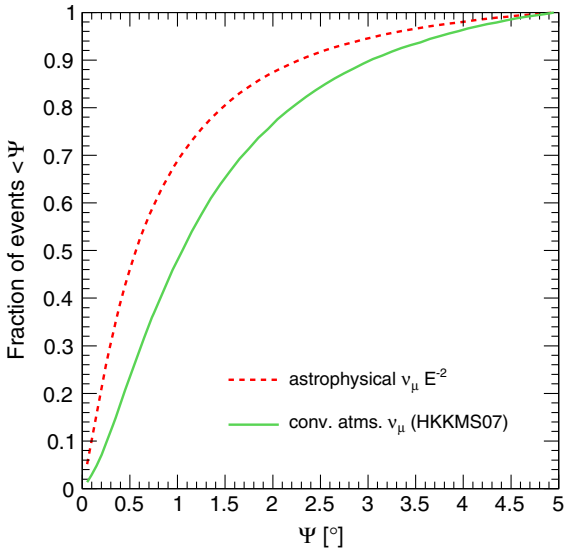

FIG. 3 (color online). The cumulative distribution of the angular resolution for astrophysical E^{-2} and conventional atmospheric events reconstructed by the MPE likelihood fit [21] obtained from Monte Carlo simulation.

$(\nu_\mu + \nu_\tau)$ at the level of the Waxman-Bahcall upper bound would correspond to about 50 events in this data sample. The contamination of background from misreconstructed atmospheric muons in this event selection is estimated from simulations. These calculations find a neutrino purity of $99.85\% \pm 0.06\%(\text{stat}) \pm 0.04\%(\text{sys})$, corresponding to a muon background of about 30 events. Based on simulation it is known that these remaining atmospheric background muons are rather low in energy and therefore have no impact on the search for an astrophysical signal in the high-energy tail.

The angular and energy resolution of events in the final event selection are illustrated in Figs. 3 and 4. Ninety percent of the conventional atmospheric neutrinos are reconstructed within 3° of their true direction and 50% within 1°. As more energetic tracks deposit more light in the optical sensors, the resolution is better for the harder energy spectrum than for atmospheric neutrinos.

A reconstruction of the neutrino energy is challenging because the detector only observes the deposited energy loss for a through-going muon [23]. This reconstruction is based on the measurement of the amount of light deposited along the track [22]. In this algorithm 40% of the DOMs with the largest measured charge have been removed for the energy loss estimation (truncated energy loss). This leads to an underestimation of the total energy loss; however, this observable is less sensitive to stochastic fluctuations in the energy loss. Figure 4 shows that the reconstructed truncated energy loss is well correlated to the true muon energy loss. This reconstructed energy loss is further correlated to the total muon energy, which is further correlated to the initial neutrino energy. The uncertainty of this relation increases with energy due to the stochastic nature of energy loss processes, and neutrinos that may generate high-energy muons at production points far from the detector.

The detection efficiency of a data sample can be expressed in terms of an effective area A_{eff}. For a neutrino flux arriving at the Earth's surface $\Phi(E_\nu)$, the mean rate R of neutrino events within a solid angle Ω and an energy interval ΔE_ν is proportional to this area:

$$R = \int d\Omega \int_{\Delta E_\nu} dE_\nu A_{\text{eff}}(E_\nu, \theta)\Phi(E_\nu, \theta). \qquad (2)$$

The effective area for this data sample is shown in Fig. 5. Overall, the effective area increases with energy. However, at very high energies, neutrinos are absorbed inside the Earth. This reduces the effective area in particular for vertically upward-going events. High-energy neutrinos are therefore expected to arrive predominantly from horizontal directions. The energy threshold of this analysis is around 100 GeV.

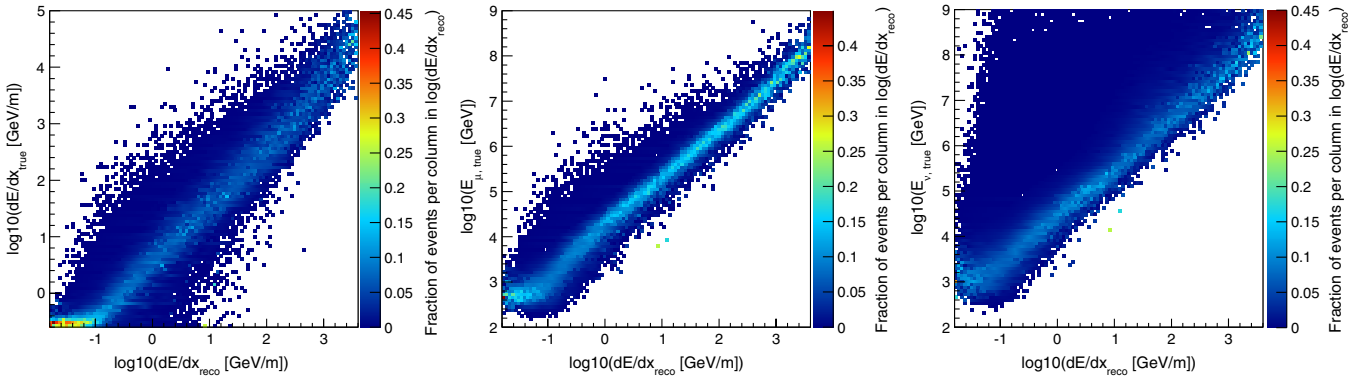

FIG. 4 (color online). Correlation between the truncated energy loss of the muon reconstructed with the algorithm Truncated Energy [22] and the true energy loss of the muon (left), the muon energy when entering the detector (middle) and the primary neutrino energy (right) obtained from Monte Carlo. The spectral shape assumed in these plots is the best-fit superposition of atmospheric and astrophysical neutrino fluxes from this analysis. Each column has been normalized individually to 1 for better visibility of the reconstruction uncertainties.

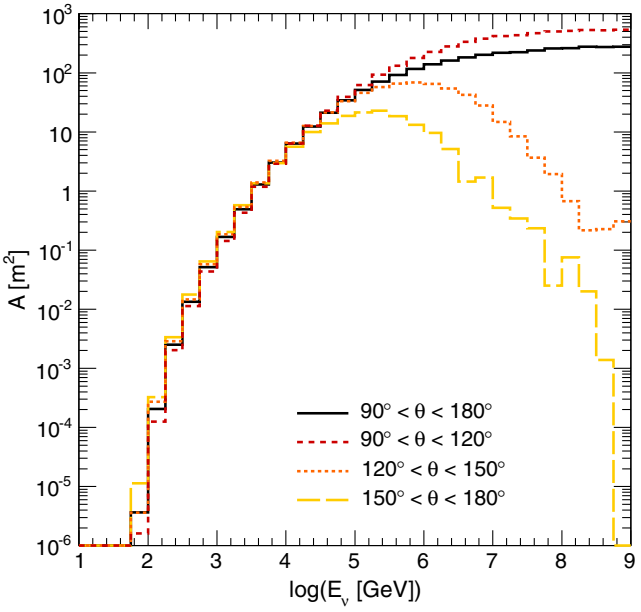

FIG. 5 (color online). Neutrino effective area averaged for ν_μ and $\bar{\nu}_\mu$ of the final event selection for different zenith bands.

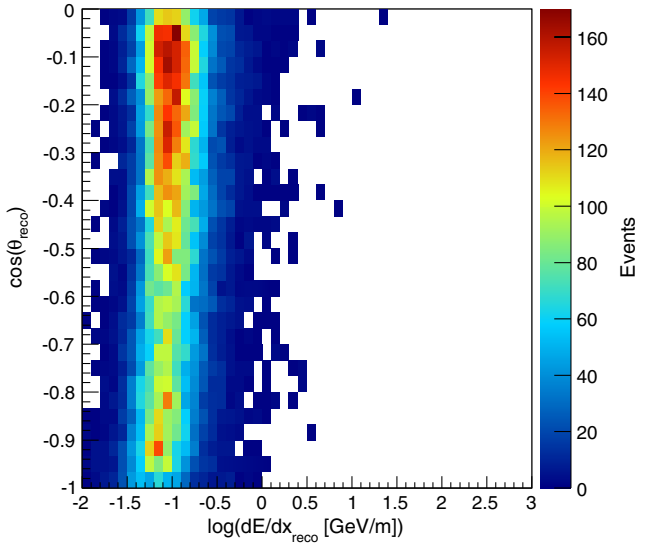

FIG. 7 (color online). Reconstructed two-dimensional distribution of truncated energy loss and zenith angle for the final event selection with 21943 events.

III. ANALYSIS METHOD

The expected distributions of deposited energy and zenith direction as well as their correlation differ for conventional, prompt and astrophysical neutrino signals. The two-dimensional probability density functions (pdfs), derived from simulation, are displayed in Fig. 6. In order to identify potential signal components among the background of conventional atmospheric neutrinos, while allowing for variation of systematic (nuisance) parameters within expected ranges, the final neutrino data sample, which is shown in Fig. 7, is analyzed with a global profile likelihood fit. This determines a global best-fit combination of neutrino flux components and nuisance parameters that is statistically consistent with the observed experimental data.

The likelihood $\mathcal{L}$ is the product of likelihoods $\mathcal{L}_{ij}$ for all bins i, j in the energy and zenith angle. The likelihood formulation chosen here is a conditional likelihood taking into account that both experimental and simulation data consist of finite statistics [36]. Here, the summed content in each bin i, j consists of d_{ij} experimentally observed data counts, and s_{ij} simulated counts, obtained from simulation with livetime different by a factor n_s to the actual experiment. Then the likelihood is defined by the ratio of the conditional binomial probabilities that the observed sum of simulation and data $s_{ij} + d_{ij}$ for each bin originates from different per-bin expectations $\mu_{s,ij} = s_{ij}/n_s$ and $\mu_{d,ij} = d_{ij}$, and the probability that they originate from the same true values $\mu_{ij} = \mu_{s,ij} = \mu_{d,ij}$. This likelihood $\mathcal{L}_{ij}$ is derived in Ref. [36] to be

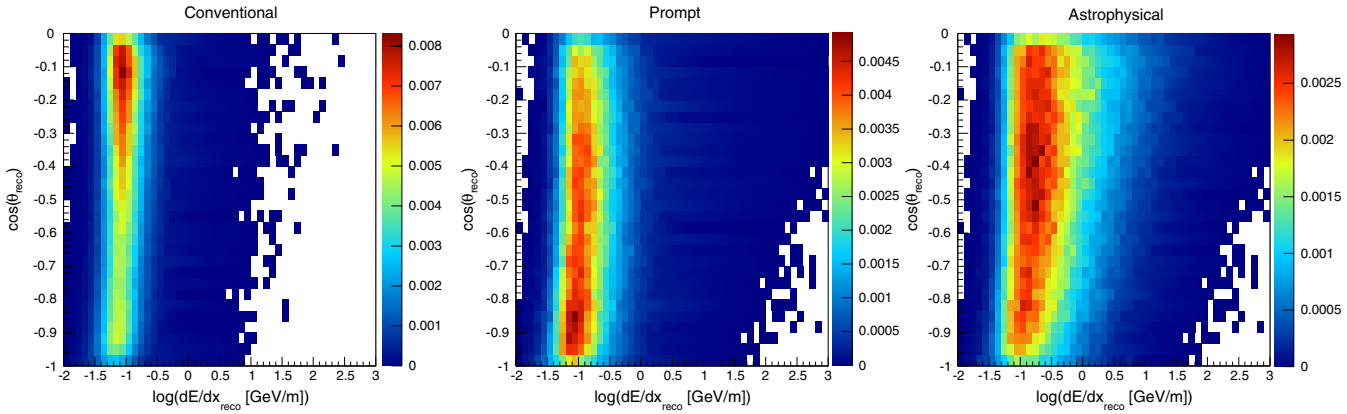

FIG. 6 (color online). Probability density functions in reconstructed truncated energy loss and cosine zenith angle for conventional atmospheric, prompt atmospheric and astrophysical neutrinos at neutrino level, each normalized to sum over all bins to unity.

$$\mathcal{L}_{ij} = \left(\frac{\mu_{ij}}{s_{ij}/n_s}\right)^{s_{ij}} \cdot \left(\frac{\mu_{ij}}{d_{ij}}\right)^{d_{ij}}. \quad (3)$$

Maximizing this likelihood results in the per-bin expectations μ_{ij} which agree best with simulation and experimental data. In case of weighted simulation, Eq. (3) has to be modified according to Ref. [36]. It is shown in [36] that for infinite simulation statistics, this likelihood converges to a saturated Poissonian likelihood ratio statistic $\mathcal{L}_{ij} = (s_{ij}/n_s)^{d_{ij}} \exp(-s_{ij}/n_s)/((d_{ij})^{d_{ij}} \exp(-d_{ij}))$, testing the observed data counts as originating from the exact simulation predictions. However, even with much larger simulation statistics than experimental data, the assumption of infinite simulation statistics is not valid for certain regions of the two-dimensional plane (see Fig. 6). Hence, the inclusion of the finite simulation statistics into the likelihood formulation has been found to improve the sensitivity of this analysis by about 10%.

The per-event expectation $\mu_{s,ij}$ for simulation is the sum of the astrophysical, prompt and conventional atmospheric neutrinos to bin (i, j),

$$\mu_{s,ij} = N_c \cdot p_{ij,c} + N_p \cdot p_{ij,p} + N_a \cdot p_{ij,a}, \quad (4)$$

where the factors p_{ij} are defined from the probability density functions (see Fig. 6). The normalization constants N_c, N_p and N_a are the parameters describing signal and background contributions to the data sample which are derived from the fit.

This formulation is designed to mitigate the effects of finite simulation statistics, which can appear with the use of two-dimensional histograms. Here, this is particularly evident in the case of the atmospheric neutrino background simulation (leftmost plot, Fig. 6). This simulation is based on a reweighting of an E^{-2} source spectrum, and provides good statistics at lower energies, compared to a choice of an E^{-1} based simulation, which, while providing a better estimate of the background at high energies, was found to provide insufficient statistics to describe the zenith angle distribution of conventional atmospheric neutrinos at lower energies. In future analyses, a weighted combination of simulation sets will be employed to exploit the best features of each, in particular, to improve the background estimate in the signal region.

Systematic uncertainties play an important role in this analysis (see Sec. IV) and are included as nuisance parameters. These are additional fit parameters which strongly suppress a bias of the signal fit result due to systematic effects. These parameters are penalized by Gaussian prior probabilities, which reflect the range of uncertainty, centered around the expectation value. Some systematic uncertainties, e.g. the assumed cosmic-ray parametrization, cannot be easily parametrized as continuous free fit parameters. In such cases, the corresponding uncertainty is still taken into account, as a discrete nuisance parameter. Then the fit is repeated with all discrete settings of the respective systematic uncertainty and the global likelihood maximum is chosen as the best fit. This implementation of nuisance parameters allows the data to constrain these combined effects while simultaneously fitting for possible signals. However, concurrent with the goal of achieving a highly unbiased result for the physics parameters, we note that these nuisance parameters can be highly correlated in their effect on the fitted observables and thus their resulting fit values cannot necessarily be interpreted individually as a measured physical value.

For hypothesis testing, a test statistic R is used, which is a likelihood ratio evaluated at a certain point $\mathbf{a}$ in the signal parameter space. R is defined as the ratio of the likelihood of best-fit signal $\hat{\mathbf{a}}$ and nuisance parameters $\hat{\mathbf{b}}$ and the likelihood of a fit with signal parameters fixed at $\mathbf{a}$ and best-fit nuisance parameters $\hat{\hat{\mathbf{b}}}$:

$$R = -2 \ln \frac{\mathcal{L}(\mathbf{a}, \hat{\hat{\mathbf{b}}})}{\mathcal{L}(\hat{\mathbf{a}}, \hat{\mathbf{b}})}. \quad (5)$$

The p-value for a certain signal hypothesis can be determined either through a full ensemble construction or through an approximation based on Wilks' theorem. For the experimental significance and upper limit calculation, the more precise full ensemble construction is used. The p-values for each signal hypothesis test are estimated through a comparison to a distribution of R from N simulated ensembles and the experimental value R_{exp} by the number N of ensemble tests with a larger R value than the experimental result:

$$\text{p-value} = \frac{N(R > R_{\text{exp}})}{N}. \quad (6)$$

A scan of the signal parameter space determines the significance and confidence region of an ensemble test or the experimental result.

For the sensitivity estimation of this analysis and additional upper limits on various signal models, the approximate and computationally faster method is used: According to Wilks' theorem, the likelihood ratio R is asymptotically χ^2 distributed, which allows a calculation of the significance [37]. However, this does not apply in a parameter space close to the physical constraints of the fit, which are that signal contributions cannot be negative. However, signal parameter points in the region of the 90% confidence level upper limits are far from the physical boundaries, and it has been verified that results based on this approximation are within 10% of the full ensemble construction.

The sensitivity of this analysis is at a flux level of $E_\nu^2 d\Phi/dE_\nu = 0.7 \times 10^{-8}$ GeV cm^{-2} s^{-1} sr^{-1}. For the first time, this search for astrophysical muon neutrinos with data from the 59-string IceCube detector achieves a sensitivity at a level about 30% below the Waxman-Bahcall upper

bound. This sensitivity includes the systematic uncertainties discussed in the following section.

IV. SYSTEMATIC UNCERTAINTIES

The determination of a possible signal component through the likelihood fit is based on the comparison of experimental data to simulation and therefore relies on a precise and well understood simulation of signal and background neutrinos. Systematic uncertainties, which affect the efficiency of the selection in the two-dimensional distribution of reconstructed energy loss and arrival direction, are therefore critical. As a prerequisite, all quality criteria, described in Sec. II, have been studied individually to check their agreement between simulation and experiment and their robustness against known systematic uncertainties.

The relevant systematic uncertainties can be grouped into two different categories: the first category (Sec. IVA) is neutrino detection uncertainties and includes uncertainties in the simulation of neutrinos, their interaction and production of secondary particles, propagation in the detection volume, and detector response. The second group (Sec. IVB) consists of uncertainties in the theoretical prediction of energy and zenith angle distributions of atmospheric background neutrinos, such as the normalization, spectral index and knee of the cosmic-ray spectrum and the pion-kaon ratio in air showers.

A. Neutrino detection uncertainties

(i) Optical efficiency of the detector
The optical efficiency includes all uncertainties concerning light production and light detection in the detector. These are the number of produced Cherenkov photons for each propagating charged particle (in particular, muons), the overall optical transparency of the ice, the ice properties inside the refrozen holes around IceCube strings, the photon detection efficiency of the photomultipliers, the photon detection efficiency of the total optical module including glass and gel transparency, i.e. its effective aperture, and the shadowing of photons by detector components, i.e. cables and the mu-metal grids. All these factors influence how bright a simulated neutrino appears in the detector. The brightness of an event is the basic information for every energy reconstruction and therefore the uncertainty of the optical efficiency results in an uncertainty on the reconstructed energy scale. Additionally, it affects the normalization and slope of the energy loss distribution, as shown in Fig. 8. The effect has been parametrized and is implemented as a continuous nuisance parameter assuming a Gaussian uncertainty of 15%.

(ii) Neutrino-nucleon cross sections
The influence of uncertainties in the differential neutrino-nucleon cross sections on the observables of this analysis is estimated through a comparison of neutrino simulations with different cross section models [38–40]. While the differences between these models are energy dependent, the effect on the observables is marginal and correlated to other uncertainties. It is therefore neglected here (see Table III).

(iii) Uncertainties on muon energy loss processes
The dominant energy loss processes in the energy range of this analysis are bremsstrahlung, pair production, and photonuclear interactions. Theoretical uncertainties are 2% for bremsstrahlung and 2.3% for pair production [25]. The uncertainties for photonuclear interactions are of the order of 5% [25,41], but photonuclear interactions contribute less to the total energy loss of the muon than bremsstrahlung. Neutrino simulations with varied cross sections of the order of the given uncertainties showed no significant effect on the observables. Expected effects are correlated to other uncertainties and the uncertainty is therefore neglected here (see Table III) and incorporated as an enhanced penalty term for the correlated uncertainties.

(iv) Optical properties of Antarctic ice
Photons produced by secondary particles in the detection volume are subject to scattering and absorption during propagation to the DOMs. The optical properties of the Antarctic ice have been estimated using calibration light sources inside the ice following two approaches [27,28] and show a

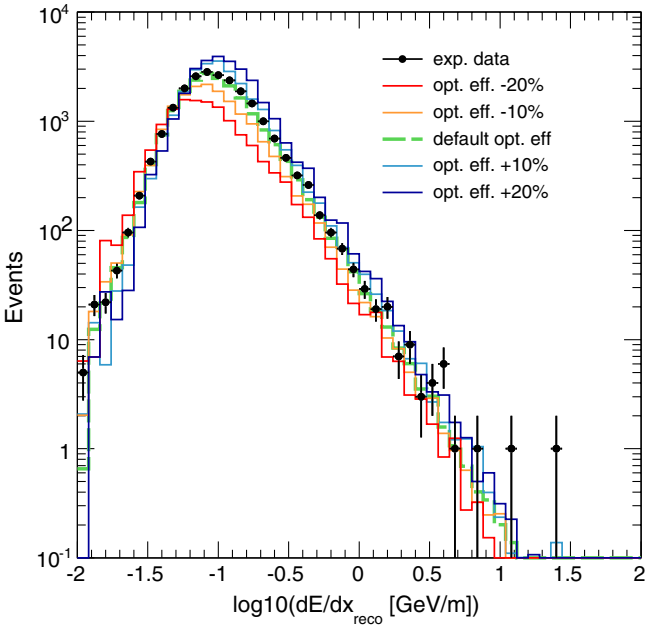

FIG. 8 (color online). The truncated energy loss distribution of events in the final event selection in comparison to simulations of conventional atmospheric neutrinos (HKKMS07 + H3a) with different settings for the optical efficiency.

TABLE III. Summary of systematic uncertainties and their implementation into this analysis. For continuous parameters constraints are implemented as a Gaussian prior around the default value with a standard deviation σ.

Uncertainty	Effect on observables	Correlated with	Implementation	default value	Constraint
Optical efficiency	shape of energy dist. norm. of energy and zenith dist.	flux normalization spectral index	continuous	1.0	$\sigma = \pm 0.15$
Neutrino-nucleon cross sections	marginal effect on slope and norm. of energy and zenith distributions	optical efficiency spectral index flux normalization	neglected		
Muon energy loss cross sections	marginal effect on slope and norm. of energy and zenith distributions	optical efficiency spectral index flux normalization	neglected		
Ice model	slope and norm. of energy and zenith distribution	flux normalization spectral index	discrete		SPICE Mie/ WHAM!
Flux normalization	norm. of energy and zenith angle distributions	optical efficiency spectral index (weakly)	continuous	1.0	$\sigma = \pm 0.3$
Knee of the cosmic-ray spectrum	slope of energy dist. minor effect on zenith angle	spectral index	discrete		H3a/poly-gonato
Change in cosmic-ray spectral index	slope of energy dist. minor effect on zenith angle	optical efficiency flux normalization (weakly)	continuous	$\Delta\gamma = 0$	$\sigma = \pm 0.1$
Pion-kaon ratio	slopes of energy and zenith angle distributions		continuous	1.0	$\sigma = \pm 0.1$

spatial dependence in particular in the vertical direction. The influence on the observables due to both ice models (SPICE Mie, WHAM!) is not parametrizable in terms of fundamental parameters and the ice model is therefore taken into account as a discrete nuisance parameter. The overall influence of the ice model uncertainty is found to be largely correlated to the flux normalization and the spectral index.

B. Atmospheric neutrino flux uncertainties

(i) Flux normalization
The uncertainty on the normalization of the conventional atmospheric neutrino background is assumed to be about 30% [14]. It is implemented as a continuous nuisance parameter with a Gaussian constraint on the conventional flux of atmospheric neutrinos. The prompt neutrino flux normalization is not constrained because it is treated as a signal parameter.

(ii) Knee of the cosmic-ray spectrum
The characteristic shape of the all-particle cosmic-ray energy spectrum with a break at the knee with an energy of 3 PeV is caused by the superposition of the spectra of different nuclei. The neutrino fluxes based on the cosmic-ray parametrizations H3a and polygonato (see the Appendix) change the atmospheric background expectation in a nontrivial way (see Fig. 13 in the Appendix): the neutrino flux expectation increases towards higher energies but is strongly reduced at highest energies due to the cosmic-ray knee. The different cosmic-ray spectra are implemented into the fit as a discrete nuisance parameter.

(iii) Cosmic-ray spectral index
Since conventional and prompt atmospheric neutrinos are produced by cosmic rays hitting the atmosphere, their energy spectrum directly depends on the energy spectrum of cosmic rays. As discussed above, the cosmic-ray nucleon spectrum, which is not a simple power law, is relevant for the neutrino flux estimation. The overall uncertainty on the spectral index is implemented as a continuous uncertainty shifting the total spectrum by $\Delta\gamma$ relative to the parametrizations of the cosmic-ray composition models discussed above. The constraint of 4% is estimated based on differences between established cosmic-ray flux parametrizations [15,34]. The sign of $\Delta\gamma$ is defined such that a positive value corresponds to a softer spectrum.

(iv) Pion-kaon ratio
The relative pion to kaon contribution to neutrino production in air showers is the main uncertainty affecting the zenith angle distribution. It is defined here as the ratio of the integrated pion and kaon neutrino flux contribution to the total neutrino flux in this data sample from Eq. (1). In the analysis, it is implemented as a continuous nuisance parameter with a Gaussian constraint of 10%. This corresponds to a 3% uncertainty in the vertical to horizontal flux ratio, which is estimated from theoretical calculations [14].

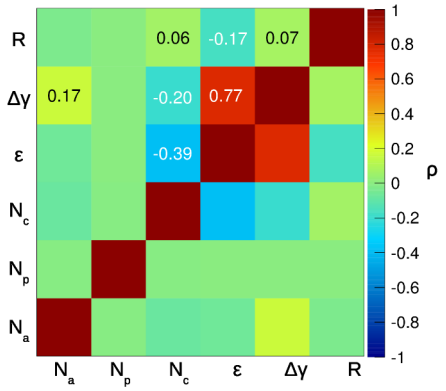

FIG. 9 (color online). Correlation coefficients between continuous-fit parameters in the fit of the experimental data. The parameters N_a, N_p, and N_c are the normalizations of astrophysical, prompt and conventional atmospheric neutrinos [see Eq. (4)]. The other parameters are the continuous nuisance parameters of the fit, i.e. the optical efficiency ϵ, the change in spectral index $\Delta\gamma$ and the pion-kaon ratio scaling factor R (see Sec. IV and Table III).

Many of these uncertainties are highly correlated in their effect on the analysis observables (see Table III and Fig. 9). The purpose of the implementation of these uncertainties as nuisance parameters in the fit is to avoid the misinterpretation of deviations between experiment and simulation due to these uncertainties as an astrophysical or prompt neutrino signal. This effect has been checked for by using simulation-based data challenges prior to the final analysis. Ensembles of experiments were generated with varying nuisance parameter settings, and then the entire fitting procedure was applied with varying assumptions on the ranges of the nuisance parameters in the fit. It was found that the procedure is very robust against nuisance parameter assumptions, and that the chance of misinterpreting systematic deviations as a signal is low.

As discussed above, the correlation between different nuisance parameters does not permit a precise determination of the corresponding physics parameters from the fit. A nuisance parameter can be absorbed by another free floating nuisance parameter describing different uncertainties if the influence on the observables is correlated. Examples are the uncertainty of quantum efficiency of optical sensors, which is correlated to the Cherenkov light yield uncertainty; and the effects of the uncertainties in the cross sections for neutrino-nucleon interactions and muon energy loss, which are fully absorbed by other parameters. For such cases only a single parameter with the combined uncertainty has been implemented into the analysis to ensure good numerical stability of the fit.

A summary of all systematic uncertainties and their implementations is given in Table III.

TABLE IV. Fit results for the fit parameters from the likelihood analysis. The results for the discrete nuisance parameters "model of optical ice properties" and "knee of the cosmic-ray spectrum" are those models which return the best likelihood value during the fit.

Fit parameter	Fit value	Statistical error on best fit	Systematic pull
Astrophys. flux [10^{-8} GeV cm^{-2} s^{-1} sr^{-1}]	0.25	$+0.70 - 0.20$	
Prompt flux N_p [ERS08 + H3a]	0	+2.41	
Optical efficiency ϵ	1.00	± 0.01	0σ
Model of optical ice properties	SPICE Mie		
Conventional flux N_c [HKKMS07 + H3a]	1.05	± 0.02	$+0.2\sigma$
Knee of the cosmic-ray spectrum	H3a		
Change in spectral index $\Delta\gamma$	−0.06	± 0.02	-0.6σ
Pion-kaon ratio scaling factor R	1.13	± 0.10	$+1.3\sigma$

V. RESULTS

A. Likelihood fit results

The two-dimensional distribution of reconstructed truncated energy loss and zenith angle for the high-purity experimental neutrino sample is shown in Fig. 7. The profile likelihood best fit of this distribution as a superposition of the three neutrino components, astrophysical, prompt atmospheric and conventional atmospheric (see Sec. III), with the nuisance parameters allowed to float within constraints (see Table III), is summarized in Table IV. The best fit for the astrophysical component is a flux of

$$E_\nu^2 \Phi(E_\nu) = 0.25 \times 10^{-8}\ \text{GeV cm}^{-2}\,\text{s}^{-1}\,\text{sr}^{-1}, \qquad (7)$$

and the best fit of the prompt atmospheric flux is zero. The projected distributions of the truncated energy loss and zenith angle are shown in Fig. 10.

All nuisance parameter best-fit values are consistent with expectations. The correlations between the continuous signal- and nuisance-fit parameters are shown in Fig. 9. Table IV shows statistical errors on the parameters of the fit, which represent the ranges allowed by the fit. The statistical error on the signal fit comes from a full ensemble construction using likelihood ratios. The statistical errors on the systematic parameters come from a standard χ^2 interpretation of the changes in likelihood from the minimum. The systematic pulls are also shown, which indicate how far the nuisance parameters have moved from their assumed baseline values. The pion-kaon ratio shows the largest pull, a 13% increase in the kaon contribution from the baseline

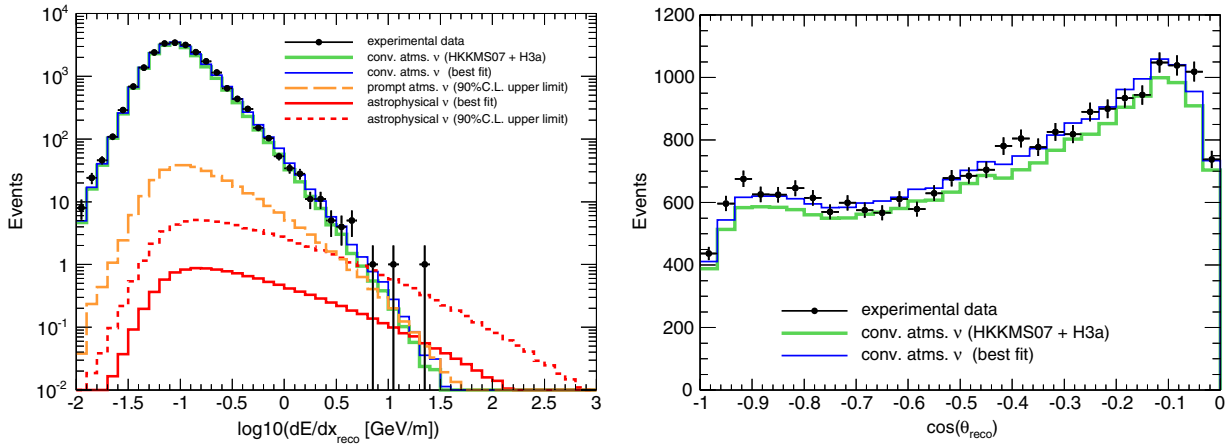

FIG. 10 (color online). Truncated energy loss and zenith angle distribution of the final neutrino data sample in comparison to the simulation of conventional atmospheric neutrinos with default nuisance parameters (green thin line) and the best-fit conventional atmospheric neutrino (blue thick line), the best fit (red solid line) and upper limit astrophysical spectra (red dashed line) and the upper limit prompt neutrino spectrum (orange long-dashed line).

assumption. This increase is not statistically significant and, due to the different sensitive energy regions of the respective analyses, cannot be directly compared to the studies of the pion-kaon ratio with atmospheric muons [42].

The fitted nonzero astrophysical signal flux is found close to the physical boundary. As the fit is constrained to non-negative signal fluxes, the significance of the likelihood ratio was determined using full ensemble constructions (see Sec. III). The hypothesis of zero signal ($\mathbf{a} = (0,0)$) results in a p-value of 0.032. This corresponds to a 1-sided significance of 1.8σ, a rejection at a 96.8% confidence level. Testing a range of values leads to the 68% confidence level allowed range for the astrophysical signal of

$$0.04 \leq \frac{E_\nu^2 \cdot \Phi(E_\nu)}{10^{-8}\ \mathrm{GeV\,cm^{-2}\,s^{-1}\,sr^{-1}}} \leq 0.94. \tag{8}$$

Furthermore, the upper limits on the astrophysical and prompt atmospheric muon neutrino fluxes were calculated using the same ensemble method. The upper limits at 90% confidence level are

$$\frac{E_\nu^2 \cdot \Phi_{\mathrm{astro}}(E_\nu)}{10^{-8}\ \mathrm{GeV\,cm^{-2}\,s^{-1}\,sr^{-1}}} \leq 1.44 \tag{9}$$

in the energy range between 34.5 TeV and 36.6 PeV and

$$\Phi_{\mathrm{prompt}}(E_\nu) \leq 3.8 \cdot \Phi_{\mathrm{ERS08+H3a}}(E_\nu) \tag{10}$$

for the baseline model ERS08 + H3a in the energy range between 2.3 TeV and 360 TeV. The sensitive energy range of the analysis is defined as the energy range which achieves a 5% worse sensitivity than the full energy range if signal pdfs are constrained from the high- and low-energy side, respectively. The best-fit and upper limit projected distributions of the reconstructed energy loss and zenith angle are illustrated in Fig. 10. An astrophysical neutrino flux at the level of the best fit would yield 12 signal neutrino events in the final neutrino data sample, and a flux at the level of the upper limit would yield 71 neutrino events. A flux at the prompt upper limit would correspond to 346 neutrinos in this data sample, which can be compared to 91 expected prompt atmospheric neutrinos assuming the ERS08 + H3a model.

B. Limits on an astrophysical E^{-2} power law flux

Figure 11 compares the upper limit of this analysis with theoretical flux predictions and limits from other experiments. The upper flux limit of this analysis is about 40% above the Waxman-Bahcall upper bound. The limit remains a factor of two above the sensitivity of this analysis due to the observed excess of high-energy events, which causes a nonzero astrophysical best-fit flux. Therefore, this optimistic scenario of highly efficient neutrino production in optically thin cosmic-ray sources cannot be excluded.

This result lowers the flux limit of the predecessor experiment AMANDA [48] by a factor of five and is a factor of three below the limit obtained by the ANTARES [49] experiment. This analysis supersedes the result of the IceCube 40-string data analysis [10]. The current study benefited from a number of improvements: in particular, a more efficient neutrino selection, the inclusion of the zenith angle into the fit and a more careful modeling of the primary cosmic-ray spectrum. Furthermore, the previous analysis overestimated its effective area, leading to an underestimated limit. The current 59-string analysis has a substantially higher sensitivity than the 40-string analysis.

IceCube analyses using the channel of cascade-like signatures have recently also found an excess of high-energy neutrino events compared to the number expected

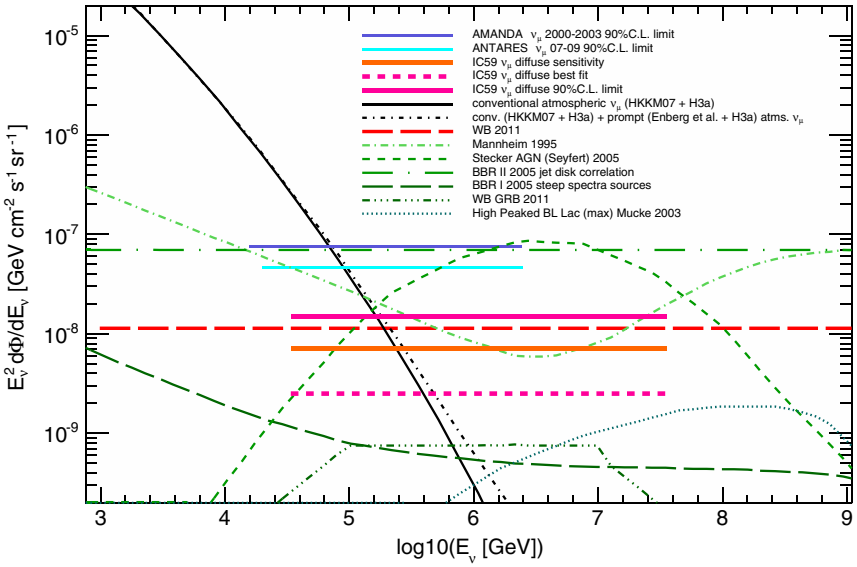

FIG. 11 (color online). Limit on a $(\nu_\mu + \bar{\nu}_\mu)$ astrophysical E^{-2} flux from this analysis in comparison to theoretical flux predictions and limits from other experiments. The black lines show the expected atmospheric neutrino flux with and without a prompt component (both without the modification of the knee feature). The red dashed line marks the Waxman-Bahcall upper bound [16,17]. Green dashed lines represent various model predictions for astrophysical neutrino fluxes [16,43–47]. Horizontal lines show limits and sensitivities from different experiments [10,48,49]. The pink solid line is the 90% confidence level (C.L.) upper limit of this analysis, the orange solid line shows its sensitivity.

from a background of neutrinos of conventional atmospheric origin. These analyses are mostly sensitive to charged-current interactions of electron neutrinos and neutral-current interactions of all neutrino flavors, while the analysis presented here is sensitive mostly to charged-current interactions of muon neutrinos. The energy resolution achieved for contained cascade-like events is better than for a through-going muon track. However, the separation of a neutrino signal from an atmospheric muon background is more challenging because of the worse angular resolution achieved in this channel. This in general leads to much smaller event samples than in the track-like channel.

Results from a search for cascade-like high-energy events with the IceCube 40-string detector configuration [8] showed a high-energy excess of events. The significance of that excess is 2.7σ with respect to the expectation of conventional atmospheric and prompt atmospheric neutrinos. The upper limit derived from that analysis is an all-flavor flux of $E_\nu^2\Phi(E_\nu) = 7.46 \times 10^{-8}\,\mathrm{GeV\,cm^{-2}\,s^{-1}\,sr^{-1}}$ (90% confidence level). Assuming equal mixing of neutrino flavors when arriving at Earth, that flux is compatible with the best-fit flux and the upper limit derived in this analysis.

The IceCube collaboration has also reported the observation of 28 high-energy events found in the search for high-energy starting events in the IceCube data taken with the IC79 configuration and the first year of the full 86-string detector [9]. These 28 events correspond to a 4.1σ excess with respect to atmospheric background and are interpreted as evidence for an astrophysical all-flavor component of $E_\nu^2\Phi(E_\nu) = 3.6 \pm 1.2 \times 10^{-8}\,\mathrm{GeV\,cm^{-2}\,s^{-1}\,sr^{-1}}$ [9]. Of these 28 events, only 7 events show a clear track-like signature; the other 21 events have the typical spherical shape of cascade-like events. Assuming again an equal mixing of neutrino flavors, the best-fit flux of the high-energy analysis corresponds to a muon neutrino flux of $E_\nu^2\Phi(E_\nu) = 1.2 \times 10^{-8}\ \mathrm{GeV\,cm^{-2}\,s^{-1}sr^{-1}}$ with a cutoff at 2 PeV. A fit with an unbroken E^{-2} signal hypothesis, as used in the analysis presented here, would yield a slightly lower astrophysical flux normalization. Such a flux level is just below the upper limit set by the muon neutrino search presented here. The best-fit astrophysical spectral index, if unconstrained in the fit, is $\gamma = 2.2$. The 28 events predominantly originate from the Southern Hemisphere, while the muon neutrino search presented here is only performed for events below the horizon with zenith angles greater than 90 degrees.

C. Limits on diffuse neutrino flux models

The experimental data are also compared to various theoretical diffuse neutrino flux models. Best-fit fluxes and upper limits on each of these models are given as a model rejection factor (MRF)[50], the ratio between the upper-limit flux assuming the shape of the model prediction and the flux predicted by the model itself. An MRF less than one implies that the model is rejected by the measurement at a confidence level of more than 90%. Models with model rejection factors greater than one are constrained by this analysis by less than 90% C.L. In order to calculate the MRFs, the baseline signal hypothesis pdf (see Fig. 6) has

TABLE V. Model rejection factors and best-fit fluxes in units of the predicted model flux for different theoretical predictions of $(\nu_\mu + \bar{\nu}_\mu)$ astrophysical neutrino fluxes.

Model	Neutrino source	Best fit $[\Phi_{\text{model}}(E_\nu)]$	MRF	Energy range
Stecker [43]	Active Galactic Nuclei (AGN) cores	0.06	0.33	216 TeV to 8.6 PeV
Mannheim [44]	jets of radio-loud AGN	0.13	0.86	28 TeV to 2.4 PeV
BBRI [45]	steep spectrum FR-II galaxies and blazars	3.77	23.07	overlap with the atmospheric range
BBRII [45]	flat spectrum FR-II galaxies and blazars	0.03	0.21	73 TeV to 8.4 PeV
Muecke *et al.* [47]	BL Lac objects	6.83	43.96	PeV to EeV energies
WB GRB [16,46]	gamma-ray bursts (GRBs)	3.74	21.72	84 TeV to 4.3 PeV

been exchanged by the two-dimensional energy loss and zenith angle distribution predicted by the corresponding model and the fit has been repeated. The best-fit flux for each model is given in Table V as the best-fit normalization of the model prediction. The MRFs given in Table V are based on a χ^2 approximation around this best-fit maximum instead of using the computing-intensive confidence interval construction following the Feldman-Cousins approach [51].

Three models are excluded by this analysis at 90% C.L.: those by Stecker, Mannheim, and the flat spectrum source model by Becker *et al*. The upper limit of this analysis is a factor of 22 above the Waxman-Bahcall model for GRBs [16,46]. The analysis presented here cannot constrain this model, but it has already been constrained by dedicated GRB searches with IceCube [52]. There is no sensitivity to the models by Muecke *et al.* [47] and the steep spectrum source model from Becker *et al.* (BBRI) [45]. The reason is that these models do not predict sufficient neutrino fluxes in the most sensitive energy range of this analysis, which is roughly the region between 100 TeV and 10 PeV. Moreover, the predicted steep spectrum of the BBRI model causes a large degeneracy between the astrophysical signal flux normalization and the atmospheric flux and nuisance parameters. Also, the model by Muecke *et al.*, which predicts a very low neutrino flux, does so only in the PeV to EeV energy range, which is beyond the reach of current experiments.

TABLE VI. Model rejection factors for different theoretical predictions of prompt atmospheric neutrino fluxes [11–13]. If not noted otherwise, these models are the original published models and have not been modified for a more accurate cosmic-ray flux parametrization. Except for the baseline model ERS08 with H3a knee, MRFs are based on a χ^2 approximation.

Model	MRF
ERS08 + H3a [13,15]	3.8
ERS08 [13]	4.8
ERS08 (max) [13]	3.8
ERS08 (min) [13]	8.2
MRS03 (GBW) [11]	9.9
MRS03 (MRST) [11]	8.0
MRS03 (KMS) [11]	8.3
BNSZ89 (RQPM) [12]	0.5
BNSZ89 (QGSM) [12]	1.8

D. Limits on prompt atmospheric neutrino fluxes

Constraining the prompt atmospheric neutrino flux is challenging, because the prompt flux is hard to distinguish from the shape of the conventional atmospheric flux. In this analysis no indications of a prompt signal are observed. The corresponding upper limit on a prompt atmospheric neutrino component can be compared to the results from the AMANDA experiment [48]. Those limits are a factor of seven less constraining than the limits set by the analysis presented here.

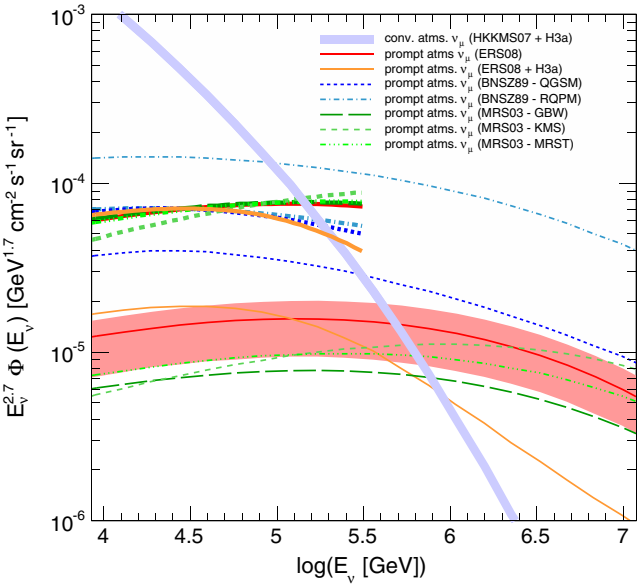

FIG. 12 (color online). Prompt atmospheric $\nu_\mu + \bar{\nu}_\mu$ neutrino fluxes in comparison to the expected flux of conventional atmospheric neutrinos (Honda *et al.* + H3a). Model predictions are represented by thin lines [11–13]. The red shaped area marks the theoretical uncertainty on the prediction of ERS08. Limits for each model are shown as thick lines in the corresponding line style and color in the valid energy range between 2.3 TeV and 360 TeV (see Table VI). The baseline model used here is the model ERS08 modified with the cosmic-ray parametrization by Gaisser *et al.* and is represented by the thick orange line. Other models are shown as published.

In addition to the limit on the baseline flux ERS08+H3a, upper limits are also calculated for other prompt neutrino flux predictions [11–13]. The results for the different models are given in Table VI and are shown in Fig. 12. The shape of all prompt models is very similar, with the largest difference in their absolute normalization. For all models, the best-fit result for the prompt neutrino component is zero. The upper limits for additional prompt flux predictions are calculated based on the Wilks' theorem and are given in units of MRF. All limits are valid in the energy range between 2.3 TeV and 360 TeV.

The upper limits derived from this analysis are typically still a factor of 4 to 10 above current prompt flux calculations based on perturbative QCD (Enberg *et al.* [13], Martin *et al.* [11]). The model rejection factor for the intrinsic charm model by Bugaev *et al.* [12] is 0.5. This means that even a flux as low as 50% of the Bugaev *et al.* prediction is excluded by this analysis with 90% C.L.

VI. CONCLUSION

For the search for a diffuse astrophysical flux of $\nu_\mu + \bar{\nu}_\mu$ a global likelihood fit of the two-dimensional distribution of measured energy loss and arrival direction of detected muon neutrino events by IceCube in its 59-string configuration was performed. In particular, the high neutrino purity of the sample and the careful treatment of systematic uncertainties of the detection method and the theoretical modeling of background in the fit allowed a substantial increase in sensitivity compared to earlier IceCube analyses. With the search presented here, a sensitivity below the Waxman and Bahcall upper bound has been achieved for the first time by a neutrino telescope.

This search found a high-energy excess of 1.8σ compared to the background scenario of a pure conventional atmospheric model. The corresponding best-fit astrophysical $\nu_\mu + \bar{\nu}_\mu$ flux is $E_\nu^2 \Phi(E_\nu) = 0.25 \times 10^{-8}\,\mathrm{GeV\,cm^{-2}\,s^{-1}\,sr^{-1}}$. The 90% confidence level upper limit on the flux is $E_\nu^2 \Phi(E_\nu) \leq 1.44 \times 10^{-8}\,\mathrm{GeV\,cm^{-2}\,s^{-1}\,sr^{-1}}$. Due to the observed excess of high-energy events, this limit is slightly above the Waxman and Bahcall upper bound.

This analysis also sets constraints on a prompt atmospheric neutrino flux. The limit on a prompt muon neutrino contribution to the data sample is $\Phi_{\mathrm{prompt}}(E_\nu) \leq 3.8 \cdot \Phi_{\mathrm{Enberg\,et\,al.+H3a}}(E_\nu)$. This limit is still a factor of 4 to 10 above pQCD model predictions [11–13], but lowers previous flux constraints by one order of magnitude [48]. The intrinsic charm model by Bugaev *et al.* is disfavored at a confidence level of more than 90%.

This result is consistent with the excess of high-energy events found in IceCube analyses searching for cascade-like signatures: an analysis with the IC40 detector found an excess of 2.7σ over the atmospheric background [8]. The recently reported evidence for an extraterrestrial neutrino flux found in a search with IceCube's IC79 and first year of IC86 configuration has a significance of 4.1σ. The upper limits and best-fit fluxes of these analyses are consistent with the IC59 analysis of track-like events presented here within their yet large uncertainties.

Future studies in all detection channels will reveal if the observed excesses can be attributed to an astrophysical neutrino signal. With a runtime of several years, the full IceCube detector will also improve its sensitivity to prompt atmospheric neutrinos and reach the sensitivity level of current prompt model predictions. The muon neutrino search presented here will profit from the larger detector providing higher statistics in particular in the high-energy region. Since high-energy neutrinos are absorbed by the Earth, the effective area for the highest-energy events is largest at the horizon. An extension of the field of view of the muon neutrino search above the horizon would increase the analysis sensitivity to an astrophysical flux. Future muon neutrino searches will reach the sensitivity to probe the astrophysical diffuse neutrino flux at the level of the high-energy starting event analysis reported in Ref. [9].

ACKNOWLEDGMENTS

We acknowledge the support from the following agencies: the U.S. National Science Foundation-Office of Polar Programs, the U.S. National Science Foundation-Physics Division, the University of Wisconsin Alumni Research Foundation, the Grid Laboratory Of Wisconsin (GLOW) grid infrastructure at the University of Wisconsin-Madison, the Open Science Grid (OSG) grid infrastructure; the U.S. Department of Energy and the National Energy Research Scientific Computing Center, the Louisiana Optical Network Initiative (LONI) grid computing resources; the Natural Sciences and Engineering Research Council of Canada, WestGrid and Compute/Calcul Canada; the Swedish Research Council, the Swedish Polar Research Secretariat, the Swedish National Infrastructure for Computing (SNIC), and the Knut and Alice Wallenberg Foundation, Sweden; the German Ministry for Education and Research (BMBF), Deutsche Forschungsgemeinschaft (DFG), Helmholtz Alliance for Astroparticle Physics (HAP), the Research Department of Plasmas with Complex Interactions (Bochum), Germany; the Fund for Scientific Research (FNRS-FWO), FWO Odysseus programme, the Flanders Institute to encourage scientific and technological research in industry (IWT), the Belgian Federal Science Policy Office (Belspo); the University of Oxford, United Kingdom; the Marsden Fund, New Zealand; the Australian Research Council; the Japan Society for Promotion of Science (JSPS); the Swiss National Science Foundation (SNSF), Switzerland; the National Research Foundation of Korea (NRF); and the Danish National Research Foundation, Denmark (DNRF).

APPENDIX: CALCULATION OF THE NEUTRINO KNEE

The effect of the knee on the neutrino spectrum is estimated relative to the initial power-law extrapolation by calculating the ratio of the neutrino flux at energy E_ν from the spectrum with the knee to that obtained from the power-law extrapolation. The calculation of Ref. [14] is taken as the default spectrum for the power-law extrapolation. The rescaling factor is given by

$$\frac{\Phi_{\nu^{\mathrm{CR}}}(E_\nu)}{\Phi_\nu^{\mathrm{HKKMS07}}(E_\nu)} = \frac{\int dE_N \Phi_{\mathrm{N\,CR}}(E_N)\frac{d}{dE_\nu}Y(E_N,E_\nu,\cos(\theta^*))}{\int dE_N \Phi_{\mathrm{N,HKKMS}}(E_N)\frac{d}{dE_\nu}Y(E_N,E_\nu,\cos(\theta^*))}, \quad \text{(A1)}$$

where $\phi_{N,\mathrm{HKKMS}}(E_N)$ is the spectrum of nucleons used in the calculation of Ref. [14] and $\Phi_{\mathrm{N\,CR}}$ is the spectrum of nucleons for a different cosmic-ray flux parametrization, here Gaisser H3a [15] or poly-gonato (modified) [34]. The yield of $\nu_\mu + \bar{\nu}_\mu$ per nucleon as a function of the neutrino energy E_ν, the nucleon energy E_N and the inclination of the cosmic ray θ^* is taken as

$$Y(E_N,E_\nu,\cos(\theta^*)) = \frac{\epsilon_\nu^*}{E_\nu\cos(\theta^*)}\cdot\left(\frac{E_N}{AE_v}\right)^p\left(1-\frac{AE_\nu}{E_N}\right)^q, \quad \text{(A2)}$$

where $\epsilon_\nu^* = 4.8$ GeV, $p = 0.76$ and $q = 5.25$.

Equation (A2) is an adaptation of the approximation originally proposed by Elbert [53] to approximate the number of muons per primary nucleon. It is based on air shower simulations (see, e.g. Refs. [54,55]). It has been checked that the formula for neutrinos is consistent with simulations with CORSIKA and SIBYLL over a range of primary energies. This rescaling method is used to take advantage of the full range of existing simulations of atmospheric neutrino induced muons in IceCube. The rescaling factors are shown in Fig. 13.

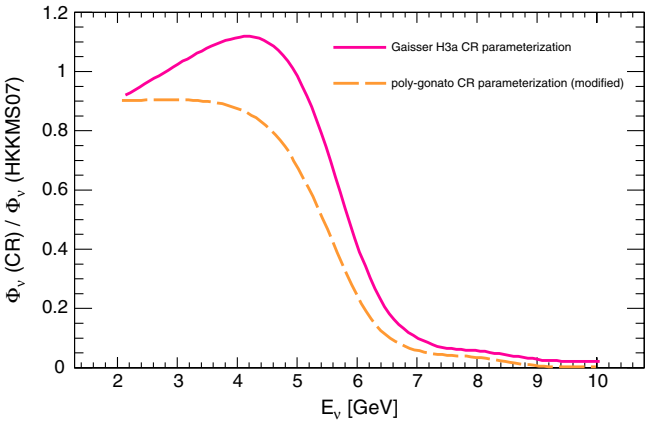

FIG. 13 (color online). Ratio of the two muon neutrino fluxes calculated based on the cosmic-ray parametrizations H3a [15] and poly-gonato (modified) [34] with knee to the standard HKKMS07 muon neutrino flux [14] as a function of energy.

Similar correction functions have also been calculated for the prompt atmospheric neutrino prediction ERS08 [13]. Since the analytical derivation of a neutrino yield factor is challenging for prompt neutrinos, the yield is calculated from air shower simulations using CORSIKA [29] with DPMJET [56,57].

[1] T. K. Gaisser, F. Halzen, and T. Stanev, Phys. Rep. **258**, 173 (1995).
[2] J. Learned and K. Mannheim, Annu. Rev. Nucl. Part. Sci. **50**, 679 (2000).
[3] J. K. Becker, Phys. Rep. **458**, 173 (2008).
[4] R. Abbasi *et al.* (IceCube Collaboration), Astrophys. J. **732**, 18 (2011).
[5] S. W. Barwick and A. Silvestri, Phys. Rev. D **81**, 023001 (2010).
[6] L. A. Anchordoqui, V. Barger, I. Cholis, H. Goldberg, D. Hooper *et al.*, arXiv:1312.6587.
[7] M. Aartsen *et al.* (IceCube Collaboration), Phys. Rev. Lett. **111**, 021103 (2013).
[8] M. Aartsen *et al.* (IceCube Collaboration), arXiv:1312.0104 [Phys. Rev. D (to be published)].
[9] M. Aartsen *et al.* (IceCube Collaboration), Science **342**, 1242856 (2013).
[10] R. Abbasi *et al.* (IceCube Collaboration), Phys. Rev. D **84**, 082001 (2011).
[11] A. Martin, M. Ryskin, and A. Stasto, Acta Phys. Pol. B **34**, 3273 (2003).
[12] E. V. Bugaev, V. A. Naumov, S. I. Sinegovsky, and E. S. Zaslavskaya, Nuovo Cimento Soc. Ital. Fis. **12C**, 41 (1989).
[13] R. Enberg, M. H. Reno, and I. Sarcevic, Phys. Rev. D **78**, 043005 (2008).
[14] M. Honda, T. Kajita, K. Kasahara, S. Midorikawa, and T. Sanuki, Phys. Rev. D **75**, 043006 (2007).
[15] T. K. Gaisser, Astropart. Phys. **35**, 801 (2012).
[16] E. Waxman and J. N. Bahcall, Phys. Rev. D **59**, 023002 (1998).
[17] E. Waxman, arXiv:1101.1155.
[18] A. Achterberg *et al.* (IceCube Collaboration), Astropart. Phys. **26**, 155 (2006).

[19] R. Abbasi *et al.* (IceCube Collaboration), Astropart. Phys. **35**, 615 (2012).
[20] R. Abbasi *et al.* (IceCube Collaboration), Nucl. Instrum. Methods Phys. Res., Sect. A **618**, 139 (2010).
[21] J. Ahrens *et al.* (AMANDA Collaboration), Nucl. Instrum. Methods Phys. Res., Sect. A **524**, 169 (2004).
[22] R. Abbasi *et al.* (IceCube Collaboration), Nucl. Instrum. Methods Phys. Res., Sect. A **703**, 190 (2013).
[23] M. Aartsen *et al.* (IceCube Collaboration), arXiv:1311.4767 [JINST (to be published)].
[24] A. Gazizov and M. P. Kowalski, Comput. Phys. Commun. **172**, 203 (2005).
[25] D. Chirkin and W. Rhode, arXiv:hep-ph/0407075.
[26] J. Lundberg, P. Miočinović, K. Woschnagg, T. Burgess, J. Adams, S. Hundertmark, P. Desiati, and P. Niessen, Nucl. Instrum. Methods Phys. Res., Sect. A **581**, 619 (2007).
[27] M. Ackermann *et al.*, J. Geophys. Res. **111**, D13203 (2006).
[28] M. Aartsen *et al.* (IceCube Collaboration), Nucl. Instrum. Methods Phys. Res., Sect. A **711**, 73 (2013).
[29] D. Heck, G. Schatz, T. Thouw, J. Knapp, and J. Capdevielle, Report No. FZKA-6019, 1998.
[30] G. Barr, T. Gaisser, P. Lipari, S. Robbins, and T. Stanev, Phys. Rev. D **70**, 023006 (2004).
[31] R. Abbasi *et al.* (IceCube Collaboration), Phys. Rev. D **83**, 012001 (2011).
[32] T. K. Gaisser, *Cosmic Rays and Particle Physics* (Cambridge University Press, Cambridge, 1990).
[33] P. Lipari, Astropart. Phys. **1**, 195 (1993).
[34] J. R. Hoerandel, Astropart. Phys. **19**, 193 (2003).
[35] A. Schukraft, PhD thesis, RWTH Aachen University, [Institution Report No. urn:nbn:de:hbz:82-opus-46898, 2013], http://darwin.bth.rwth-aachen.de/opus3/volltexte/2013/4689/.
[36] D. Chirkin, arXiv:1304.0735.
[37] S. S. Wilks, Ann. Math. Stat. **9**, 60 (1938).
[38] H. L. Lai, J. Huston, S. Kuhlmann, J. Morfin, F. Olness, J. F. Owens, J. Pumplin, and W. K. Tung (CTEQ Collaboration), Eur. Phys. J. C **12**, 375 (2000).
[39] A. Cooper-Sarkar and S. Sarkar, J. High Energy Phys. 01 (2008) 075.
[40] A. Cooper-Sarkar, P. Mertsch, and S. Sarkar, J. High Energy Phys. 08 (2011) 042.
[41] I. A. Sokalski, E. V. Bugaev, and S. I. Klimushin, in *Proceedings of the 2nd Workshop of Methodical Aspects of Underwater/Ice Neutrino Telescopes*, edited by R. Wischnewski (DESY Zeuthen, Hamburg, Germany, 2002).
[42] E. W. Grashorn, J. K. de Jong, M. C. Goodman, A. Habig, M. L. Marshak, S. Mufson, S. Osprey, and P. Schreiner, Astropart. Phys. **33**, 140 (2010).
[43] F. W. Stecker, Phys. Rev. D **72**, 107301 (2005).
[44] K. Mannheim, Astropart. Phys. **3**, 295 (1995).
[45] J. K. Becker, P. L. Biermann, and W. Rhode, Astropart. Phys. **23**, 355 (2005).
[46] E. Waxman and J. N. Bahcall, Phys. Rev. Lett. **78**, 2292 (1997).
[47] A. Muecke, R. Protheroe, R. Engel, J. Rachen, and T. Stanev, Astropart. Phys. **18**, 593 (2003).
[48] A. Achterberg *et al.* (IceCube Collaboration), Phys. Rev. D **76**, 042008 (2007).
[49] J. Aguilar *et al.* (ANTARES Collaboration), Phys. Lett. B **696**, 16 (2011).
[50] G. C. Hill and K. Rawlins, Astropart. Phys. **19**, 393 (2003).
[51] G. J. Feldman and R. D. Cousins, Phys. Rev. D **57**, 3873 (1998).
[52] R. Abbasi *et al.* (IceCube Collaboration), Nature (London) **484**, 351 (2012).
[53] J. Elbert, "Multiple Muons Produced by Cosmic Ray Interactions," in *Proceedings DUMAND Summer Workshop, La Jolla, California, 1978*, edited by A. Roberts, UHE Interactions, Neutrino Astronomy Vol. **2** (DUMAND Scripps Institution of Oceanography, La Jolla, California, 1979), pp. 101–121.
[54] T. Gaisser and T. Stanev, Nucl. Instrum. Methods Phys. Res., Sect. A **235**, 183 (1985).
[55] C. Forti, H. Bilokon, B. d'Ettorre Piazzoli, T. Gaisser, L. Satta, and T. Stanev, Phys. Rev. D **42**, 3668 (1990).
[56] G. Battistoni, C. Bloise, C. Forti, M. Greco, J. Ranft, and A Tanzini, Astropart. Phys. **4**, 351 (1996).
[57] P. Berghaus, T. Montaruli, and J. Ranft, J. Cosmol. Astropart. Phys. 06 (2008) 003.